Estimates of cloud radiative forcing in contrail clusters using GOES imagery

David P. Duda

Center for Atmospheric Sciences, Hampton University, Hampton, Virginia

Patrick Minnis

Atmospheric Sciences, NASA Langley Research Center, Hampton, Virginia

Louis Nguyen

Analytical Services and Materials, Inc., Hampton, Virginia

Abstract. Using data from the Geostationary Operational Environmental Satellite (GOES), the evolution of solar and longwave radiative forcing in contrail clusters is presented in several case studies. The first study examines contrails developing over the midwestern United States in a region of upper tropospheric moisture enhanced by the remnants of Hurricane Nora on September 26, 1997. Two other cases involve contrail clusters that formed over the Chesapeake Bay and the Atlantic Ocean on February 11 and March 5, 1999, respectively. The last study includes contrails forming over the tropical Pacific near Hawaii. Observations of tropical contrails near Hawaii show that the contrail optical properties are similar to those measured from satellite in the midlatitudes, with visible optical depths between 0.3 and 0.5 and particle sizes between 30 and 60 μm as the contrails mature into diffuse cloudiness. Radiative transfer model simulations of the tropical contrail case suggest that ice crystal shape may have an important effect on radiative forcing in contrails. The magnitudes of the observed solar and longwave radiative forcings were 5.6 and 3.2 W m^{-2} less than those from the corresponding model simulations, and these differences are attributed to the subpixel scale low clouds and uncertainties in the anisotropic reflectance and limb-darkening models used to estimate the observed forcing. Since the broadband radiative forcing in contrails often changes rapidly, contrail forcing estimates based only on the polar orbiting advanced very high resolution radiometer (AVHRR) data could be inaccurate due to the lack of sufficient temporal sampling.

1. Introduction

Clusters of spreading, persistent contrails sometimes form in heavy air-traffic regions when the warm exhaust emissions from subsonic jet aircraft mix with cold and relatively moist ambient air in the upper troposphere. Time series of satellite imagery have shown that these clusters can develop into large regions of cirrus-like cloudiness [Minnis et al., 1998a], which may affect climate by modifying the atmospheric radiative budget. As contrails are ice clouds, they have radiative effects that are similar to thin cirrus clouds [Fu and Liou, 1993] and may have significant regional climatic impacts [Liou et al., 1990].

Brasseur et al. [1998] have summarized recent research on the climatic impact of contrails. They concluded that the effects of persistent contrails on global climate may become important if global contrail coverage continues to increase as expected. However, Brasseur et al. cautioned that their conclusions were highly uncertain due to a lack of knowledge about the size of the areas affected by persistent contrail formation and even the sign of the radiative forcing (cooling or warming). The current best estimate of global mean contrail coverage is about 0.1%, while the best estimate of global contrail radiative forcing (0.02 W m^{-2} warming) is uncertain to a factor of 5 due to uncertainties in contrail coverage and optical depth. Although this radiative forcing is small compared to the forcing due to other anthropogenic changes in the twentieth century (1.5 W m^{-2}) [Meerkötter et al., 1999], recent projections of future air traffic suggest that contrail radiative forcing may be as large as 0.1 W m^{-2} by the year 2050 [Minnis et al., 1999].

A few studies have investigated the radiative forcing properties of contrails using radiative transfer models [e.g., Fortuin et al., 1995; Meerkötter et al., 1999]. These studies show that the net radiative forcing of contrail clusters can be positive or negative, depending on the particle size spectra and the optical thickness of the clouds. Since these cloud properties often depend on the age of the contrails, estimates of cloud radiative forcing throughout the lifetime of the cloud system are necessary to assess the overall radiative impact of contrail clusters. Studies of contrail evolution will also improve still uncertain estimates of contrail cover and contrail optical depth values.

Using data from the Geostationary Operational Environmental Satellite (GOES), we investigate the evolution of solar and longwave radiative forcing in contrail clusters over the continental United States and Hawaii. The first study examines contrails developing over the midwestern United States in a

region of upper tropospheric moisture enhanced by remnants of Hurricane Nora on September 26, 1997. The second and third cases involve clusters of contrails that formed over the Chesapeake Bay and off the coast of Virginia on February 11 and March 5, 1999, respectively. The final case studies contrails observed near Hawaii on April 27, 1999. Time series of broadband cloud-forcing estimates are presented, comparing the cloud forcing as the contrail clusters change from linear contrails into cirrus-like cloudiness.

2. Data and Methodology

Half-hourly, 4-km infrared (IR) (10.7 μm), split window (WS) (12.0 μm), and visible (VIS) (0.65 μm) data from GOES-8 and GOES-10 were used to track the evolution of several contrail clusters over the United States and the adjacent oceans. The contrails were detected by visual inspection and appear as cold linear features in the IR or IR/WS brightness temperature difference imagery. When they were identified, an analysis box was drawn around the cluster, and the clouds were tracked over a period of 2–5 hours. The circumscribed areas were analyzed with the layer bispectral threshold method (LBTM) of *Minnis et al.* [1995] to estimate cloud fraction C, optical depth τ, cloud center and top temperatures T_c and T_t, and cloud top heights z_t during the daytime for solar zenith angles $\theta_0 < 78°$. The LBTM cloud amounts are based on the fraction of pixels having IR temperatures $T < T_{cs} - \Delta T$ and VIS reflectance $\rho > \rho_{cs} + \Delta\rho$, where ΔT and $\Delta\rho$ are the clear-sky tolerances following *Minnis et al.* [1995], and the subscript cs refers to clear-sky values. The cloud properties are determined for each pixel in three layers: low, middle, and high with altitude boundaries $z < 2$ km, $2 \leq z \leq 6$ km, and $z > 6$ km, respectively. Optical depth is derived for low and midlevel clouds using a reflectance model that assumes water droplets having an effective radius of 10 μm. High cloud optical depths are based on a cirrostratus cloud having idealized randomly oriented, hexagonal ice columns with an effective diameter of about 41 μm [*Minnis et al.*, 1993]. If a value for τ is derived, an IR emittance is computed, and the observed IR temperature is adjusted to determine T_c when the cloudy pixel is semitransparent. An additional adjustment is applied to estimate T_t for optically thin clouds. The values of T_c and T_t are identical when the cloud is optically thick. If τ is unavailable, T_c is equal to the IR temperature T. Soundings from rawinsondes launched nearby or within each case study region were used to initialize the LBTM. In each case study, the cloud-forcing analysis was simplified by selecting contrails that appeared in otherwise cloud-free regions such that contrail-only radiative forcing estimates could be made.

The reflectances for the GOES VIS channel are computed from

$$\rho = \frac{\pi L_v}{E_8 \cos \theta_0 \delta(d) \chi(\mu_0, \mu, \phi)}, \quad (1)$$

where the observed radiance is $L_v = a_0 + a_1 CT$, CT is the 10-bit count, d is the day of the year, δ is the Earth-Sun distance correction factor, E_8 is the solar constant for the GOES VIS channel, μ_0 and μ are the cosines of the solar and satellite zenith angles, ϕ is the relative azimuth angle between Sun and satellite, and χ is the anisotropic directional model which depends on the background. The values for χ were taken from the models of *Minnis and Harrison* [1984]. The calibration

coefficients a_0 and a_1 were determined for both satellites from calibrations among the GOES imagers, the advanced very high resolution radiometer (AVHRR) on the NOAA polar orbiting satellites, and the Visible and Infrared Scanner (VIRS) onboard the Tropical Rainfall Measuring Mission (TRMM) satellite [*Nguyen et al.*, 1999]. The calibration coefficients change over time for each satellite. For the cases involving the GOES-8 satellite, the coefficients a_0 and a_1 are -21.8 and 0.764, respectively, for the Hurricane Nora case, -24.0 and 0.842 for the February 11, 1999 case, and -24.1 and 0.845 for the March 5, 1999 case. For the April 27, 1999, case with the GOES-10 satellite, the coefficients a_0 and a_1 are -17.4 and 0.601, respectively. For the longwave channels, the nominal GOES calibrations were used to convert IR counts to temperatures.

The VIS reflectances and IR temperatures were converted to VIS albedo α_v and IR flux F_{ir}, respectively, as in the work of *Minnis et al.* [1995]. These values were then converted to a broadband solar (0.2–5.0 μm) albedo α_{sw} and longwave (5–50 μm) flux F_{lw} using empirical relationships based on correlations between coincident GOES and Earth Radiation Budget Experiment (ERBE) satellite data over the tropical ocean [*Doelling et al.*, 1998b] (for the solar data) and *Minnis et al.* [1991] (for the longwave data). These conversion formulae are

$$\alpha_{sw} = 0.0571 + 0.7198\alpha_v + 0.0287\alpha_v^2 + 0.0523 \ln(1/\mu_0),$$
$$(2)$$

$$F_{lw} = 101.32 + 3.829F_{ir} + 0.0076F_{ir}^2 - 0.2009 \ln(RH),$$
$$(3)$$

where μ_0 is the cosine of the solar zenith angle, RH is the mean relative humidity of the altitude $z(T_m)$, and T_m is the mean IR temperature in the analysis box. Similar formulae were used to convert GOES-10 radiances to broadband albedo and flux quantities. *Minnis et al.* [1991] show that for instantaneous GOES measurements the root-mean-square difference between the longwave flux derived from (3) and coincident ERBE broadband flux measurements is 10.0 W m^{-2}. The relative differences (random error) in the broadband shortwave albedos derived from (2) from ScaRaB (Scanner for Radiation Budget) measurements and coincident aircraft measurements are less than 10% [*Doelling et al.*, 1998a]. During the Atmospheric Radiation Measurement Enhanced Shortwave Experiment (ARESE) campaign the GOES-8-derived albedos over Oklahoma were 0.013 ± 0.016 greater than the albedos measured from the high-altitude ER-2 aircraft [*Valero et al.*, 2000].

Solar top of atmosphere (TOA) shortwave cloud radiative forcing (SWCRF) is computed as

$$SWCRF = E_0(\delta)\mu_0(\alpha_{clr} - \alpha_{cld}), \quad (4)$$

while the longwave cloud radiative forcing (LWCRF) is

$$LWCRF = F\uparrow_{clr} - F\uparrow_{cld}, \quad (5)$$

where E_0 is the solar constant in W m^{-2}, α_{clr} is equal to the mean clear-sky solar albedo of the box (as determined by LBTM), α_{cld} is the mean cloudy-sky albedo in the box, and $F\uparrow_{clr}$ and $F\uparrow_{cld}$ are the mean clear and cloudy-sky upward longwave fluxes. Differencing the clear- and cloudy-sky fluxes results in a radiative forcing estimate for 100% cloud cover. Since most scenes contain only high level clouds, the radiative forcing estimates assume 100% contrail cover. The effects of

low clouds on the radiative forcing estimates are discussed later.

The areal coverage of the contrails was computed from the LBTM cloud coverage estimates using the equation

$$\text{Area} = \text{area (km)} \times \text{number of cloudy pixels},$$
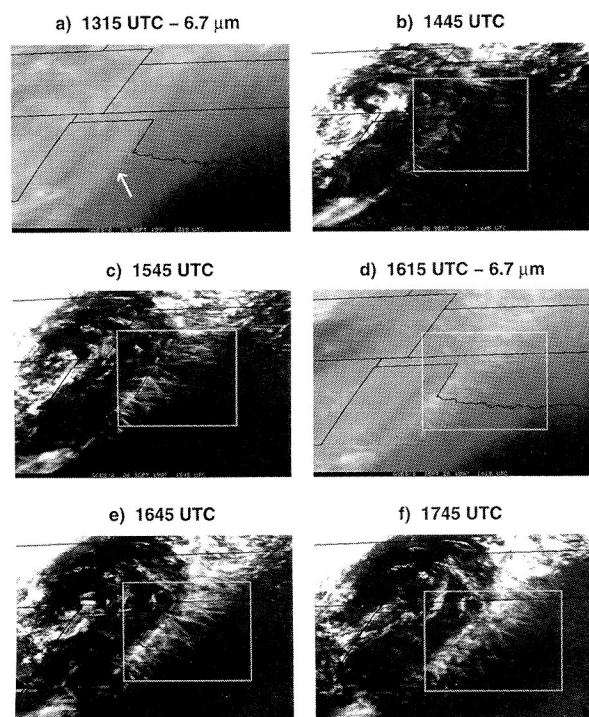
where the pixel area is determined from the pixel resolution (computed by Man computer Interactive Data Access System (McIDAS) software [*Lazzara et al.*, 1999]) at the center of the analysis box. The pixel resolution at nadir for the IR channel is 4.01 km $\times$ 2.29 km [*Space Systems/Loral*, 1996], while elsewhere it is roughly equal to the nadir pixel area divided by the cosine of the satellite-viewing zenith angle.
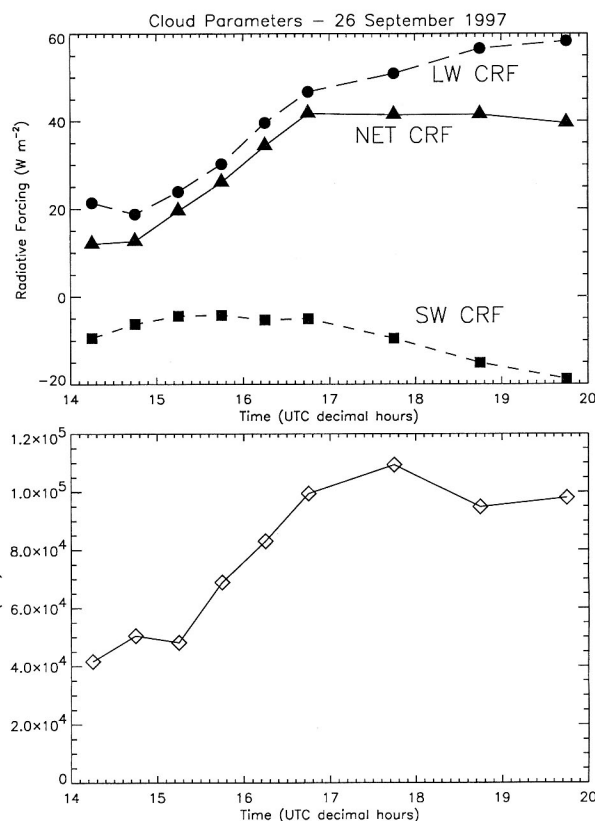
3. Results

Four cases of contrail clusters are presented below. The first occurred on September 26, 1997 over Texas, Oklahoma, and Kansas, while the second cluster formed over Maryland and Virginia and, subsequently, drifted over the Atlantic on February 11, 1999. The third case describes a rapidly growing contrail cluster that developed off the coast of Virginia on March 5, 1999. The final cluster of contrails formed west of Hawaii on April 27, 1999. Time series of cloud radiative forcing are presented for each case, with discussion focusing on the temporal variability of the forcing.

3.1. September 26, 1997

Figure 1 shows GOES IR and 6.7-μm water vapor imagery of a large number of contrails developing along a line from Kansas to northern Texas between 1315 and 1745 UTC on

Figure 2. Time series of broadband radiative forcing (long-wave, solar, and net) for 100% cloud cover and areal contrail coverage for the areas described in Figure 1.

Figure 1. Enhanced GOES-8 4-km IR and 6.7 μm water vapor imagery of contrails forming over Oklahoma, Texas, and Kansas on September 26, 1997. (a) The arrow shows the tongue of upper level moisture where the contrail clusters form. (b–f) The boxes show the extent of the analysis box.

September 26, 1997. These contrails formed in a region of upper tropospheric moisture that was enhanced by the remnants of Hurricane Nora (see Figure 1a). The influence of the moisture on contrail development is evident in this case, as an outbreak of persistent contrails over such a large area of the United States during September is unusual. Surface observations over the United States [*Minnis et al.*, 1997] indicate a minimum in contrail frequency during September.

Time series of both solar and longwave radiative forcing and areal contrail coverage are presented in Figure 2. Because of the warm surface and a relatively dry lower troposphere the net (=solar + longwave) radiative forcing is dominated by longwave forcing and becomes as large as +40 W m^{-2} by 1645 UTC (1145 LT). The large positive radiative forcing remains even as the contrails mature and thicken during the early afternoon leading to solar forcing as large as -20 W m^{-2}. The areal coverage of the contrails quickly grows beyond 1×10^5 km^2 by 1700 UTC. This amount of contrail coverage is extremely large, as recent estimates of the mean global persistent contrail coverage range from only 2.5×10^5 km^2 [*Ponater et al.*, 1996] to 4.6×10^5 km^2 [*Minnis et al.*, 1999]. Additionally, the box used for the coverage estimate does not include all of the contrails over the Great Plains that day.

3.2. February 11, 1999

Another large outbreak of contrails occurred during the morning of February 11, 1999. The contrails formed over the mid-Atlantic states between 1100 and 1200 UTC, then drifted over the Chesapeake Bay and eventually over the Atlantic. To

a) 1245 UTC

b) 1415 UTC

c) 1545 UTC
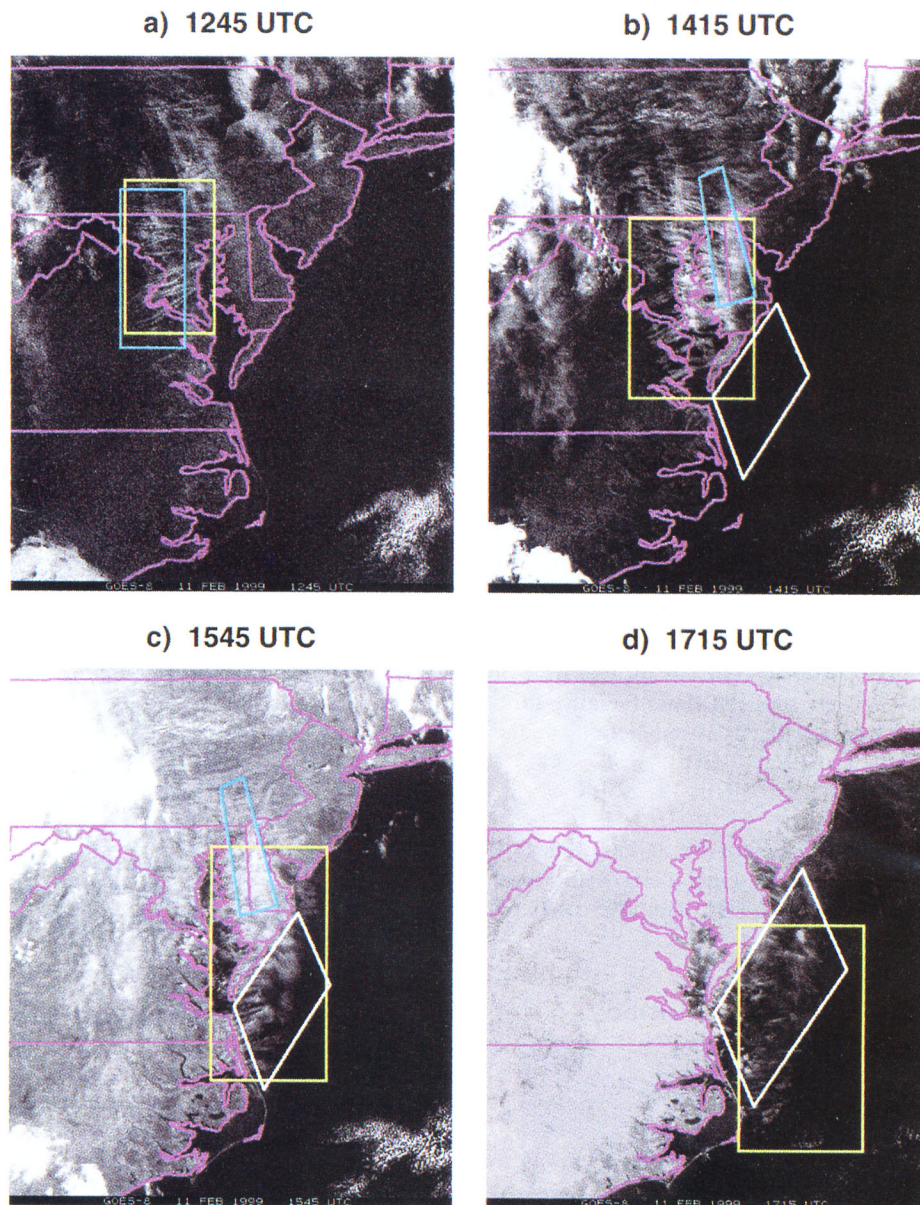
d) 1715 UTC

Plate 1. Enhanced GOES-8 1-km VIS imagery of contrails forming over the mid-Atlantic coast of the United States on February 11, 1999, between 1245 and 1715 UTC. The blue polygons indicate the areas used to compute radiative forcing over land, while the white polygons indicate the areas used to compute radiative forcing over ocean. The yellow boxes indicate the regions used to compute the areal coverage of the contrails.

contrast the effects of contrails over land and ocean, separate analysis boxes were drawn over each background. Enhanced VIS imagery of the contrails and the land and ocean analysis boxes are shown in Plate 1.

Time series of the radiative forcings are presented in Figure 3. Unlike the other case studies, individual parts of the contrail clusters were not tracked over time since the contrails drifted over a variable land/ocean background. Instead, boxes were selected over land and ocean separately, and the forcings were computed for both conditions. The net radiative forcing over land and ocean is similar. Over land, the forcing levels out after 1400 UTC (0900 LT) with a net forcing around $+10$ W m^{-2}. At 1645 UTC the solar forcing decreases as the cloud thins out and the net forcing increases to $+20$ W m^{-2}. Over the ocean the net forcing slowly increases over time and reaches $+10$ W m^{-2} after 1715 UTC (1215 LT). The contrails that formed over central Mary-

land (the yellow boxes in Plate 1) grew rapidly in areal coverage (see Figure 3), steadily increasing from 10,000 km^2 at 1245 UTC to a peak near 42,000 km^2 at 1545 UTC, then decreasing back to 20,000 km^2 by 1815 UTC. As seen in the images, the contrail coverage in the boxes is only part of the contrail outbreak which extends up to New York.

3.3. March 5, 1999

Figure 4 shows enhanced IR imagery of a contrail cluster observed during the morning of March 5, 1999, off the coast of Virginia. The contrails grew rapidly in number and coverage between 1245 and 1345 UTC. Areal coverage increases from 1000 km^2 to nearly 22,000 km^2 by 1415 UTC. After 1415 UTC the contrails began to encroach on an area of stratus, making further contrail-only radiative forcing analysis impossible. The contrail radiative forcing and areal coverage time series for the
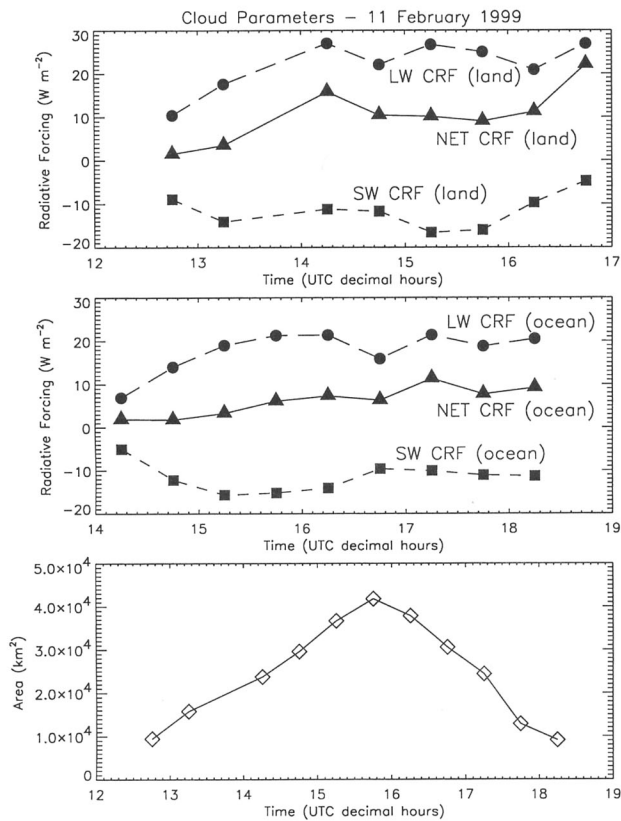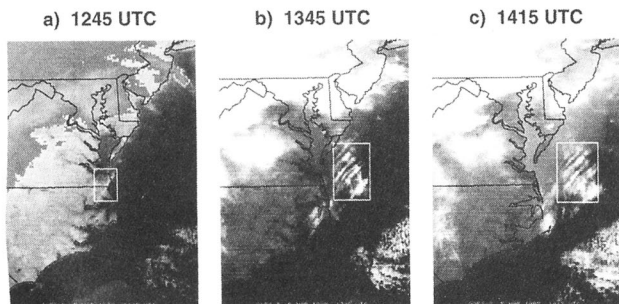
Figure 3. Time series of broadband radiative forcing (longwave, solar, and net) and areal contrail coverage for the areas described in Plate 1.

Figure 5. Time series of broadband radiative forcing (longwave, solar, and net) and areal contrail coverage for the areas described in Figure 4.

March 5 case are presented in Figure 5. The radiative forcing is once again dominated by the longwave forcing, and the net forcing grows rapidly from 3 to 25 W m^{-2} as the cloud system drifts over warm Gulf Stream waters by 1415 UTC.
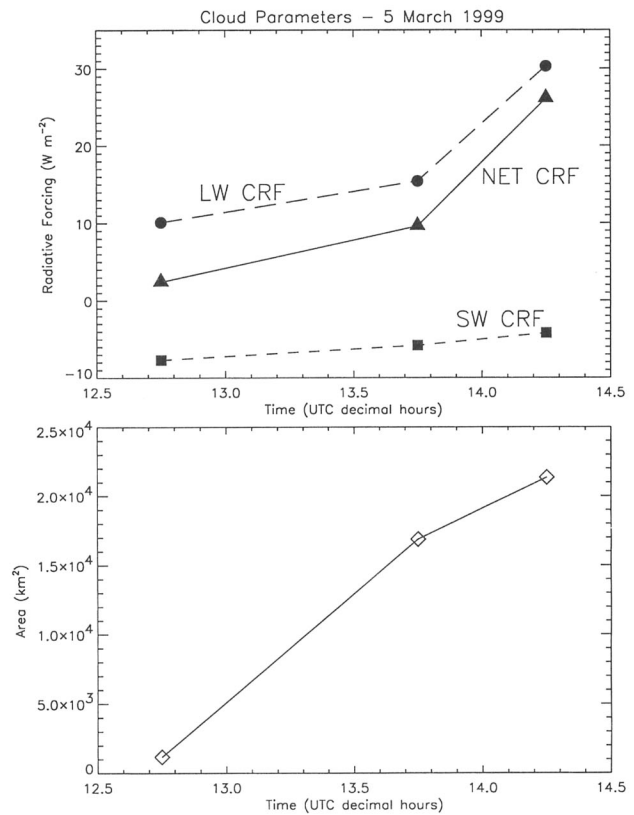
3.4. April 27/28, 1999

In Figure 6, a time series of GOES-10-enhanced IR imagery shows contrails that formed near Hawaii on April 27, 1999. This case is of particular interest because tropical contrails have rarely been studied. If significant differences between the optical properties of midlatitude and the tropical contrails were found, they would influence global estimates of contrail radiative forcing.

Two regions containing linear contrails were selected for closer study. The regions preceded a frontal zone northwest of the
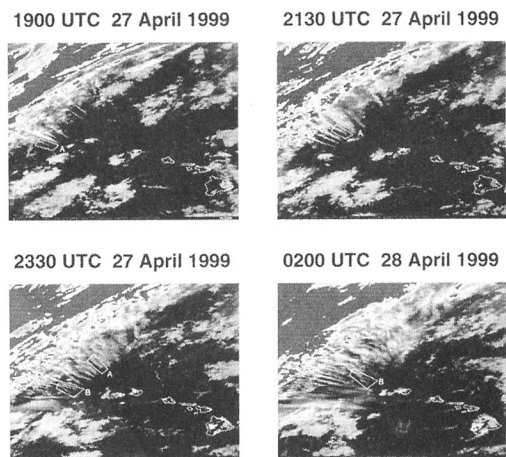
Hawaiian Islands. The first region containing three linear contrails (Region A) was tracked at half-hour intervals between 1900 and 0000 UTC (0900 and 1400 LT), while a second region containing two contrails (Region B) was tracked from 2330 to 0430 UTC (1330 to 1830 LT). Figure 6 shows that by the end of each tracking period the contrails have evolved into diffuse, cirrus-like cloud fields. Several other contrails also formed in the area, and at times, the overall contrail coverage reached 40,000 km^2.

Figure 4. Enhanced GOES-8 4-km IR imagery of contrails forming off the coast of Virginia on March 5, 1999, between 1245 and 1415 UTC.

Figure 6. Enhanced GOES-8 4-km IR imagery of contrails forming near Hawaii on April 27/28, 1999, between 1900 and 0200 UTC. The analysis Regions A and B are labeled in each figure.
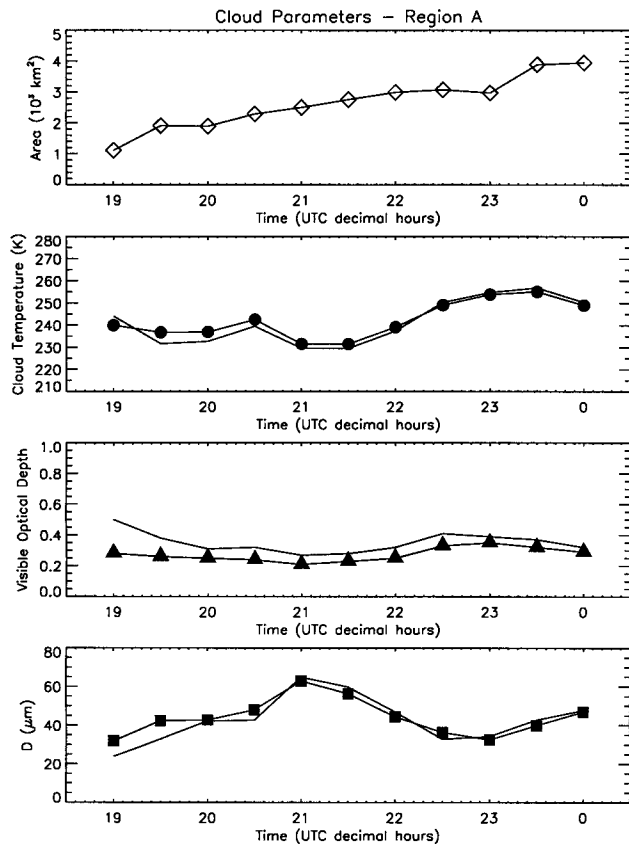
Figure 7. Time series of cloud properties (areal coverage, cloud temperature, cloud optical depth, and particle size) for Region A described in Figure 6. The lines with symbols include all cloudy pixels with estimated heights above 6 km, while the lines without symbols exclude pixels at the edges of the contrails.

Figure 7 shows the results of cloud parameters computed using the VIS-IR-SI technique (VIST) [*Minnis et al.*, 1995] in Region A. The VIST uses an iterative technique to simultaneously determine effective ice particle diameter (D_e), VIS optical depth (τ), and cloud temperature (T_c) given the observed VIS reflectance (ρ), the SI and IR brightness temperatures and estimates of the clear-sky reflectance (ρ_{cs}), and SI and IR clear-sky brightness temperatures. Temperatures and reflectances for a range of particle sizes and optical depths are computed for the given solar zenith, viewing zenith, and relative azimuth angles, $(\theta_0, \theta, \text{and } \phi, \text{respectively})$, using the cloud emittance and reflectance parameterizations of *Minnis et al.* [1998b] and a VIS surface-atmosphere-cloud reflectance parameterization [*Minnis et al.*, 1995]. The cloud parameters are determined by iteratively solving for the best match between the observed and the modeled temperatures and reflectances. Effective ice particle diameters for the particle distributions used in the VIST models are calculated by

$$D_e = \frac{\int D^2 LN(L)\, dL}{\int DLN(L)\, dL}, \qquad (6)$$

where L is the particle length, D is the particle width, and N is the normalized number of particles in a size bin.

The contrails in the analyzed box expand over time resulting in the areal coverage increasing from 1100 km^2 at 1900 UTC to 4000 km^2 at 0000 UTC. Cloud temperature ranges from 235 to 255 K, with the warmest temperatures occurring as the areal coverage peaks. The cloud temperatures are overestimated as most contrails form in commercial flight routes between 8 and 11 km where temperatures range from 223 to 248 K according to a sounding from Kauai, Hawaii. *Minnis et al.* [1998a] noted a similar cloud temperature overestimation by VIST, and suggested several causes, including partially filled pixels, errors in the retrieved VIS and IR optical depths due to differences between the actual and the modeled cloud particle shapes, and decrease in the average cloud height produced by the sedimentation of large particles from the contrails. This sedimentation into the slower-moving lower layers is responsible for the rapid spreading of the contrails [e.g., *Jensen et al.*, 1998]. By the time the contrail is obvious in the 4-km GOES IR data, it has already undergone considerable sedimentation and spreading. The retrieved visible optical depth changes little over the analysis period, remaining between 0.2 and 0.35. The cloud particle size increases from 32 μm at 1900 UTC to a maximum of 63 μm at 2100 UTC, then decreases back to 46 μm by 0000 UTC. Also shown in Figure 7 (lines without symbols) are the cloud parameters derived after removing the pixels at the edge of each contrail. This attempt to minimize the effects of partly cloudy pixels on the retrievals is discussed later. The cloud particle sizes and optical depths derived for these tropical contrails are similar to those retrieved from midlatitude contrails. *Minnis et al.* [1998a] report that midlatitude contrails measured during the Subsonic Cloud and Contrail Effects Special Study (SUCCESS) campaign had optical depths ranging from 0.2 to 0.8 and cloud particle sizes between 20 and 90 μm. Similar values were retrieved from the midlatitude cases in this study (not shown).

The cloud parameters retrieved for Region B are shown in Figure 8. The areal coverage peaks at 4500 km^2 by 0030 UTC and is only 2200 km^2 by 0430 UTC. The retrieved cloud temperatures range between 243 and 254 K. The visible optical depth remains nearly constant (between 0.25 and 0.35) throughout the tracking period. Retrieved cloud particle sizes show an upward trend over time, increasing from 29 μm at 2330 UTC to 59 μm at 0400 UTC.

Time series of the cloud radiative forcing for both regions are presented in Figure 9. The longwave forcing in Region A was remarkably constant throughout the analysis period, remaining near 15–17 W m^{-2}, while the solar forcing ranged from 2 to -10 W m^{-2}. Since the cloud optical depth remained relatively constant during the period, the changes in SWCRF are mostly caused by changes in cloud particle size. This is reflected in the correlation between the retrieved particle size in Figure 7 and the SWCRF in Figure 9. Since cloud reflectance is inversely related to cloud particle size, it follows that the SWCRF would decrease (increase) in magnitude with increasing (decreasing) cloud particle size. The net CRF throughout the period ranged from 3 to 18 W m^{-2}. The LWCRF in Region B is also fairly constant, ranging from 13 to 18 W m^{-2} and is possibly influenced by low clouds between 0130 and 0300 UTC. At 2330 UTC the solar forcing in Region B is near zero and is a result of the effects of partially filled pixels on the solar forcing. As the contrails mature, the solar forcing increases until after 0200 UTC when the solar zenith angle becomes important. The net CRF varies from -2 to 15 W m^{-2}.

4. Comparison of Observed and Calculated Radiative Forcing

Meerkötter et al. [1999] presented a systematic study of the radiative forcing in contrails. They simulated the forcing over a wide range of atmospheric conditions and cloud properties using three different radiative transfer models. In this section we compare our observed forcing estimates from the April 27/28, 1999, case with those calculated from one of the models used in the Meerkötter et al. study (Fu and Liou model [*Fu and Liou*, 1993; *Liou et al.*, 1998]).

For a better comparison between the observed cloud forcing and the results from the radiative transfer model, the pixels at the edge of each contrail were excluded from the satellite retrievals. The edge pixels are more likely to contain partly cloudy pixels than those at the center of the contrail, and bias the forcing estimates relative to the model calculations which assume a uniform cloud cover. Using the LTBM high-cloud mask, the pixels that were completely surrounded by other cloudy pixels were kept, while all others were discarded. The results of using the nonedge pixels in the contrail radiative forcing estimates are also shown in Figure 9. In Region A the observed LWCRF increased, on average, from 16.0 to 21.1 W m^{-2}, while the mean SWCRF over the tracking period changed from -5.0 to -13.6 W m^{-2}, resulting in a decrease in the net forcing from 11.0 to 7.5 W m^{-2}. For Region B the differences are smaller but show the same qualitative result: the mean LWCRF increased from 15.3 to 18.0 W m^{-2}, and the observed SWCRF decreased from -9.6 to -14.6 W m^{-2} with a decrease in the net CRF from 5.7 to 3.4 W m^{-2}. The largest differences between the all-cloud/nonedge cloud results occur
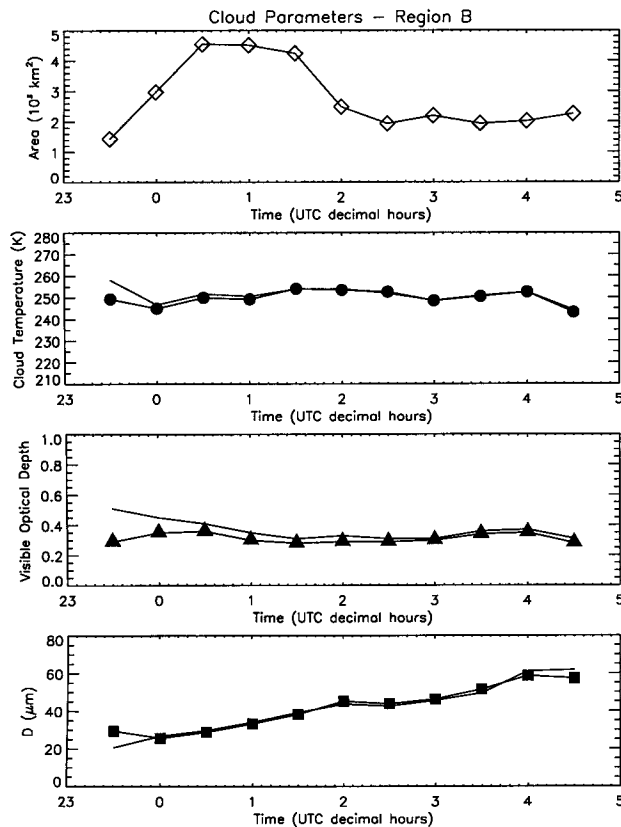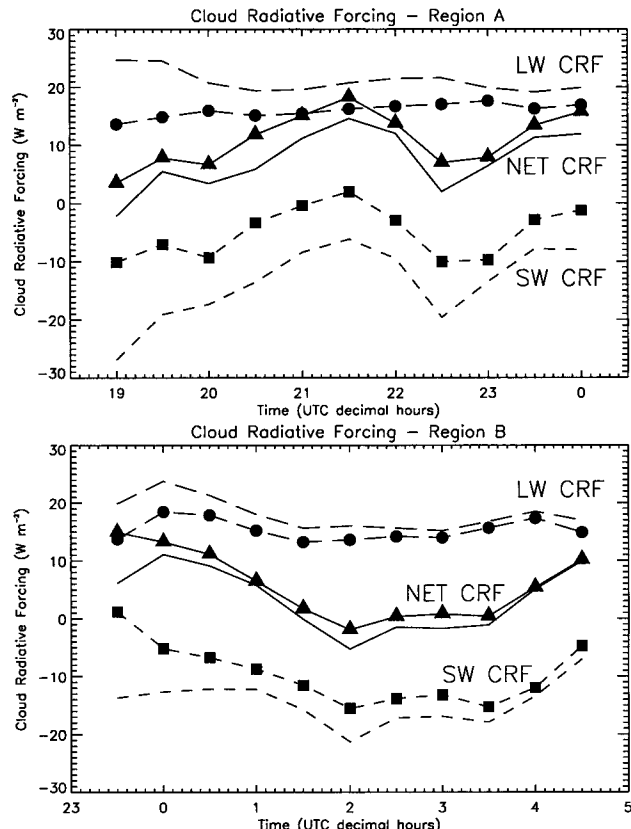

Figure 9. Time series of broadband radiative forcing (long-wave, solar, and net) and areal contrail coverage for the areas described in Figure 6. The lines with symbols include all cloudy pixels with estimated heights above 6 km, while the lines without symbols exclude edge pixels.

at the beginning of each analysis period when the clouds are narrower and the analysis regions are more likely to contain partly filled pixels.

Selecting the nonedge pixels also affected the retrieved cloud properties, as shown in Figures 7 and 8. Using only nonedge pixels tended to increase optical depth but produced little change in particle size. For example, in Region A the mean optical depth over the tracking period changed from 0.27 to 0.35 by excluding the edge pixels. The corresponding optical depths in Region B changed from 0.31 to 0.37. The mean particle sizes only decreased by 1 μm or less in both regions, from 44.0 to 42.8 μm in Region A and from 41.6 to 41.3 μm in Region B.

The Fu and Liou model calculations were run using a composite of the moisture and temperature soundings taken from the island of Kauai between 1200 UTC, April 27, 1999 to 1200 UTC, April 28, 1999. The sea surface temperature was estimated from the Channels 4 and 5 brightness temperatures using the daytime MCSST algorithm from *McClain et al.* [1985]. The surface albedo was set as a function of solar zenith angle following *Payne* [1972]. Maritime aerosol with an optical depth of 0.08 was added to the model atmosphere. The Fu and Liou model computed a clear-sky outgoing longwave flux within 2 W m^{-2} of the satellite-observed value. The top of the contrail was placed at a height in the model matching the cloud temperature retrieved from VIST (11 km or roughly 230 K), and the cloud thickness was set to 200 m.

Figure 8. Same as Figure 7 but for Region B.
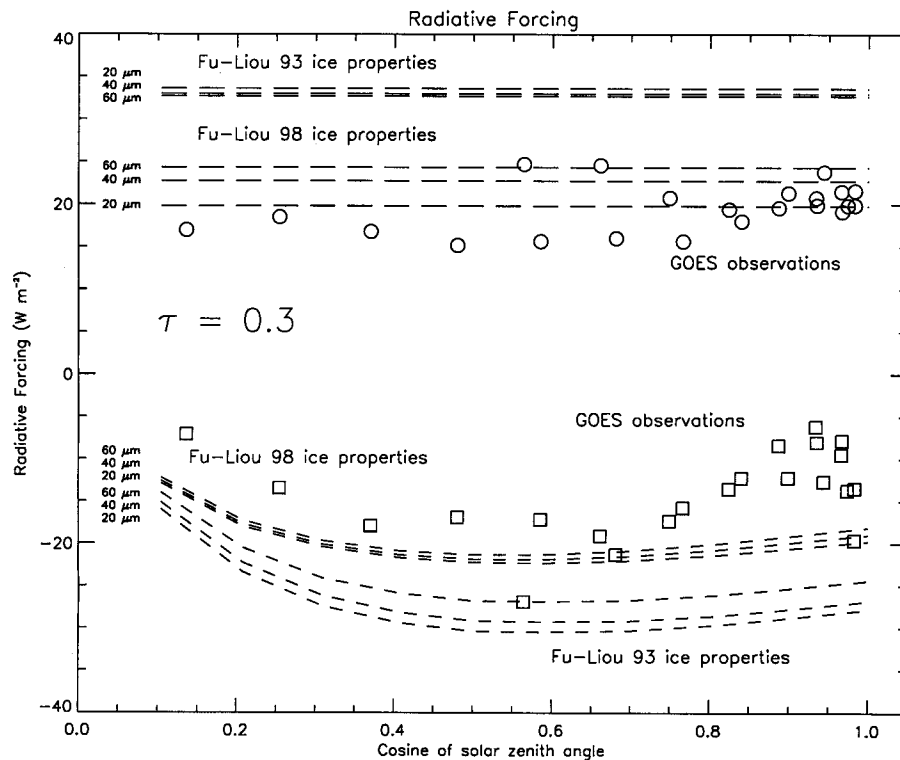
Figure 10. Contrail solar and longwave radiative forcing as a function of solar zenith angle. The lines are values computed using the Fu-Liou model with ice properties from *Fu and Liou* [1993] and *Fu et al.* [1998] with mean effective sizes of 20, 40, and 60 μm. The squares are the shortwave cloud radiative forcing estimated from GOES observations, while the circles are the corresponding longwave cloud radiative forcing observations.

A comparison between the observations and the model calculations is shown in Figure 10. Two sets of model calculations were run using the original ice radiative properties presented by *Fu and Liou* [1993] (hereinafter referred to as FL93) and more recent ice properties from *Fu et al.* [1998] (hereinafter F98). As the definition of the generalized effective size used in the newer parameterization is different from the mean effective size defined in FL93, the sizes used in the F98 run were adjusted to agree with the sizes from FL93 using the formula

$$D_{ge} = -2.4 + 0.7566D_e + 9.22 \times 10^{-4}D_e^2, \qquad (7)$$

where D_{ge} is the generalized effective size used in F98, and D_e is the mean effective size used in FL93.

Figure 10 shows that the change in ice radiative properties from FL93 to F98 has a large effect on the calculated radiative forcing in both the solar and the longwave bands. For a contrail with a visible optical depth of 0.3 and an effective size of 40 μm, the computed LWCRF decreased 10 W m^{-2}, and the SWCRF increased in magnitude from 2.6 to 7.8 W m^{-2}, with the largest differences occurring for large μ_0. These changes are larger than the variations in radiative forcing resulting from particle size differences. Because much of the change in the ice radiative properties between FL93 and F98 results from changes in the ice particle shapes used in the calculations (FL93 uses hexagonal columns, while F98 uses spheroids), ice particle shape has a significant influence on cloud radiative forcing. The radiative forcing estimated from both analysis regions is also plotted in Figure 10 as a function of μ_0. The calculations using the F98 ice properties agree better with the observations than the FL93 properties, but the LWCRF is still overestimated as much as 7 W m^{-2}, and the SWCRF is underestimated as much as 13 W m^{-2}. The differences in SWCRF appear to be largest for large values of μ_0. The differences between the observed and the calculated net CRF (not shown) are often less than ±5 W m^{-2} since the solar and longwave forcing differences tend to cancel each other.

Averaging over both analysis regions, the mean observed SWCRF in the April 27/28, 1999, case was −14.1 W m^{-2}, while the mean observed LWCRF was 19.5 W m^{-2}. The 24-hour mean of the net CRF is computed as the mean SWCRF multiplied by the daytime fraction (0.54), plus the mean LWCRF, and is equal to 11.9 W m^{-2}. The 24-hour mean therefore computes the net radiative forcing assuming that the contrail remains unchanged over the 24-hour period [*Meerkötter et al.*, 1999; *Minnis et al.*, 1999]. The 24-hour mean computed using FL93 ice properties is 18.8 W m^{-2}, while it is 12.1 W m^{-2} using F98 ice properties. *Meerkötter et al.* [1999] computed a daily mean TOA contrail forcing of 31.5 W m^{-2} over tropical oceans assuming hexagonal ice particles such as those used in the FL93 ice properties. Meerkötter et al. assumed a visible optical depth of 0.57 compared to 0.3 in this study. For small optical depths the net cloud forcing scales nearly linearly with optical depth, so adjusting the results to $\tau = 0.3$ would give a net forcing of 16.6 W m^{-2}, similar to the calculated results here for FL93 ice properties.

One possible reason for the differences between the observed and the calculated contrail radiative forcings may be the presence of low clouds below the contrails. As shown by
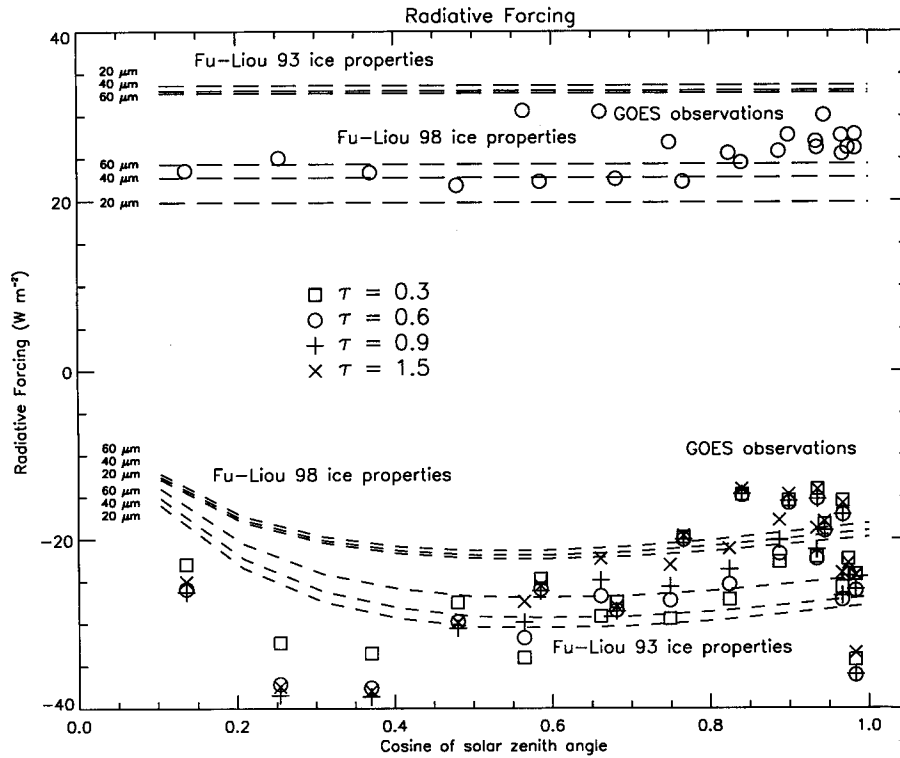
Figure 11. Same as Figure 10 but using GOES observations converted to fluxes using a limb-darkening model and anisotropic directional reflectance model developed for optically thin cirrus.

Meerkötter et al. [1999], the effect of low clouds below contrails is to decrease the magnitudes of both the SWCRF and the LWCRF, with the largest changes in the solar forcing, leading to a net increase in the radiative forcing. Although the analysis regions were chosen to minimize low-cloud amount and pixels determined from LBTM to have low cloud were excluded, it is possible some subpixel scale low cloud may have affected the results.

The estimates of α_{sw} and F_{lw} for the observed contrails may also be biased because of the models used to correct for anisotropic reflectance and limb darkening. For example, the anisotropic bidirectional reflectance models used to convert the reflectance to narrowband albedo [*Minnis and Harrison*, 1984] were derived for an average overcast cloud, while the contrails are optically thin. Thin clouds have less multiple scattering, and therefore their scattering patterns are more like the single crystal phase function and hence more anisotropic than their thick counterparts. Similarly, thin cirrus clouds are cold and produce much more limb darkening than thick high clouds, thin low clouds, or the average conditions used in the applied limb-darkening model.

Adjustments to the anisotropic directional reflectance and limb-darkening models were made to simulate optically thin cirrus clouds. Using the VIS optical depth/emissivity relationship for cirrostratus clouds of *Minnis et al.* [1993],

$$\varepsilon = 1 - \exp[-0.471(\tau_{vis}/\mu)^{1.010}],$$

where μ is the cosine of the viewing zenith angle, a new limb darkening function was created assuming a cloud optical depth of 0.3, a cloud temperature of 230 K, and a surface temperature of 293.25 K. The resulting function is approximated as

$$\gamma_n = \min[1, 0.295665 + 2.39191 \cos \theta - 3.00831 \cos^2 \theta$$
$$+ 1.32838 \cos^3 \theta],$$

and the narrowband IR flux following *Minnis et al.* [1991] is

$$F_{ir} = 2L_n(0°) \int_0^{2\pi} \int_0^{\pi/2} \gamma_n \sin \theta \cos \theta \, d\theta,$$

$$= 5.768L_n(0°),$$

where L_n is the narrowband IR radiance. Adding-doubling calculations of broadband solar albedo and reflectance from thin cirrostratus clouds were used to create a new anisotropic directional model χ for the contrails. The adding-doubling model used the same solar zenith angle-dependent surface albedos as described above, an aerosol optical thickness of 0.05, and cloud optical depths ranging from 0.3 to 1.5. The cloud radiative forcings derived using the modified limb darkening and anisotropic directional reflectance models are presented in Figure 11. The average longwave radiative forcings increased to 25.9 W m^{-2}, in between the forcings computed with both ice property models but closer to those using the F98 ice properties. The new χ factors improved the agreement between the observed and the computed solar radiative forcings for large μ_0, but the observed solar radiative forcings at large solar zenith angles were much larger than the computed values.

It is clear from Figure 11 that the new anisotropic directional reflectance model contains more anisotropy than the empirical *Minnis and Harrison* [1984] model. Considering the better agreement in the shape of the solar forcing curves in Figure 10

compared to Figure 11, the new model also contains more anisotropy than the Fu and Liou model. What is less clear is whether the new model overestimates this anisotropy, but some evidence suggests that the new cloud forcings are most likely overestimated at large solar zenith angles due to the plane-parallel assumptions used in the adding-doubling computations. *Barker* [1996] has shown that albedos calculated from a plane-parallel model are usually larger than those computed using a model with a more realistic cloud optical depth distribution. Barker found that for optically thin clouds the relative bias is largest for large solar zenith angles. *Stuhlmann et al.* [1985] compared bidirectional reflectances derived from Nimbus 7 observations with plane-parallel theoretical results. For high clouds and large solar zenith angles, they found significantly less anisotropy in the satellite observations compared to the radiative transfer results and attributed the difference to the three-dimensional structure of clouds.

The 24-hour mean in the net CRF computed from the results in Figure 11 is 12.7 W m^{-2}. Since the changes resulting from the new limb darkening and anisotropic reflectance models compensated each other, the change in the 24-hour mean was only 0.8 W m^{-2}.

5. Summary and Concluding Remarks

Time series of radiative forcing from four cases of extensive contrail coverage were presented. The solar forcing usually ranged from -5 to -15 W m^{-2} with the largest forcings often occurring after the contrails had started to become diffuse. The longwave forcing was usually larger (10 to 30 W m^{-2}) over land where the surface would become warm and could be as large as 60 W m^{-2}. However, the LWCRF was also large in the March 5, 1999, case when the contrails drifted over the Gulf Stream. Observations of tropical contrails near Hawaii show that the contrail optical properties are similar to those measured from satellites in the midlatitudes, with visible optical depths between 0.3 and 0.5 and particle sizes between 30 and 60 μm as the contrails mature into diffuse cloudiness. The cloud radiative forcing in the tropical contrails was compared to radiative transfer simulations using two different sets of ice optical properties. The observed 24-hour mean net cloud radiative forcing in the tropical contrails was nearly identical to the forcing calculated from the Fu and Liou radiative transfer model using the most recent ice crystal radiative properties from *Fu et al.* [1998], although the magnitudes of the mean observed solar and longwave forcings were 5.6 and 3.2 W m^{-2} less than the corresponding calculations, respectively. The difference between the two sets of calculated mean solar and longwave forcings were even larger (6.6 and 10.3 W m^{-2}, respectively), which suggests that the microphysical properties of contrails, including ice crystal shape, have an important effect on radiative forcing. The differences between the observed and calculated forcing may be caused by subpixel scale low clouds and the anisotropic reflectance and limb darkening models used to estimate the observed forcing. New anisotropic reflectance and limb-darkening models based on thin cirrus clouds increased the magnitude of the solar and longwave forcings 10.3 W m^{-2} and 6.3 W m^{-2}, respectively, although the solar forcing at large solar zenith angles appears to have been overestimated due to the plane-parallel assumptions used in the new model. More comparisons between observed and modeled contrail radiative forcing in tropical and midlatitude contrails are needed to reduce some of the uncertainty in estimating the magnitude of

global contrail radiative forcing and assess the competing impacts of optical depth and three-dimensional inhomogeneity on the anisotropy of the bidirectional reflectance models used to compute the albedo of contrail clusters from GOES observations.

The cases described here show that contrail areal coverage is variable and that individual clusters of linear contrails can grow larger than 100,000 km^2. As recent estimates of global contrail coverage range from 250,000 to 450,000 km^2, periodic outbreaks of contrail clusters will probably increase global coverage beyond these amounts and, consequently, increase global contrail radiative forcing.

The results from the September 26, 1997 and March 5, 1999, cases show that the net top of atmosphere (TOA) radiative forcing from contrails can also change rapidly. Contrail-forcing estimates from geostationary satellites can be a valuable supplement to those provided by polar orbiting advanced very high resolution radiometer (AVHRR) data. Because of the limited temporal resolution of the polar orbiting satellites, estimates of contrail-induced forcing, based on AVHRR data alone, could be inaccurate since contrails can have a large variation in coverage and forcing.

References

Barker, H. W., A parameterization for computing grid-averaged solar fluxes for inhomogeneous marine boundary layer clouds, part I, Methodology and homogeneous biases, *J. Atmos. Sci., 53,* 2289–2303, 1996.

Brasseur, G. P., R. A. Cox, D. Hauglustaine, I. Isaksen, J. Lelieveld, D. H. Lister, R. Sausen, U. Schumann, A. Wahner, and P. Wiesen, European scientific assessment of the atmospheric effects of aircraft emissions, *Atmos. Environ., 32,* 2327–2422, 1998.

Doelling, D. R., L. Nguyen, W. L. Smith Jr., and P. Minnis, Comparison of ARM GOES-derived broadband albedos with broadband data from ARM-UAV and ScaRaB, in *Proceedings of Eighth Atmospheric Radiation Measurement (ARM) Science Team Meeting,* pp. 201–205, U.S. Dep. of Energy, Tucson, Ariz., 1998a.

Doelling, D. R., P. Minnis, R. Palikonda, and D. A. Spangenberg, Validation of broadband fluxes derived from GMS during TOGA/COARE, in *Proceedings of CLIVAR/GEWEX COARE98 Conference,* Natl. Inst. of Stand. and Technol., Boulder, Colo., *WCRP-107, WMO/TD-940,* pp. 241–242, World Meteorol. Organ., Geneva, 1998b.

Fortuin, J. P. F., R. van Dorland, W. M. F. Wauben, and H. Kelder, Greenhouse effects of aircraft emissions as calculated by a radiative transfer model, *Ann. Geophys., 13,* 413–418, 1995.

Fu, Q., and K.-N. Liou, Parameterization of the radiative properties of cirrus clouds, *J. Atmos. Sci., 50,* 2008–2025, 1993.

Fu, Q., P. Yang, and W. B. Sun, An accurate parameterization of the infrared radiative properties of cirrus clouds for climate models, *J. Clim., 11,* 2223–2237, 1998.

Jensen, E. J., A. S. Ackerman, D. E. Stevens, O. B. Toon, and P. Minnis, Spreading and growth of contrails in a sheared environment, *J. Geophys. Res., 103,* 31,557–31,568, 1998.

Lazzara, M. A., J. M. Benson, R. J. Fox, D. J. Laitsch, J. P. Rueden, D. A. Santek, D. M. Wade, T. M. Whittaker, and J. T. Young, The Man computer Interactive Data Access System: 25 years of interactive processing, *Bull. Am. Meteorol. Soc., 80,* 271–284, 1999.

Liou, K.-N., S. C. Ou, and G. Koenig, An investigation of the climatic effect of contrail cirrus, in *Air Traffic and the Environment: Background, Tendencies, and Potential Global Atmospheric Effects,* edited by U. Schumann, pp. 154–169, Springer-Verlag, New York, 1990.

Liou, K.-N., P. Yang, Y. Takano, K. Sassen, T. Charlock, and W.

Arnott, On the radiative properties of contrail cirrus, *Geophys. Res. Lett.*, *25*, 1161–1164, 1998.

McClain, E. P., W. G. Pichel, and C. C. Walton, Comparative performance of AVHRR-based multichannel sea surface temperatures, *J. Geophys. Res.*, *90*, 11,587–11,601, 1985.

Meerkötter, R., U. Schumann, D. R. Doelling, P. Minnis, T. Nakajima, and Y. Tsushima, Radiative forcing by contrails, *Ann. Geophys.*, *17*, 1080–1094, 1999.

Minnis, P., and E. F. Harrison, Diurnal variability of regional cloud and clear-sky radiative parameters derived from GOES data, part III, November 1978 radiative parameters, *J. Appl. Meteorol.*, *23*, 1032–1052, 1984.

Minnis, P., D. F. Young, and E. F. Harrison, Examination of the relationship between outgoing infrared window and total longwave fluxes using satellite data, *J. Clim.*, *4*, 1114–1133, 1991.

Minnis, P., K.-N. Liou, and Y. Takano, Inference of cirrus cloud properties using satellite-observed visible and infrared radiances, part I, Parameterization of radiance fields, *J. Atmos. Sci.*, *50*, 1279–1304, 1993.

Minnis, P., et al., Cloud optical property retrieval (Subsystem 4.3), Clouds and the Earth's Radiant Energy System (CERES) algorithm theoretical basis document, Cloud analyses and radiance inversions (subsystem 4), *NASA Ref. Publ. 1376*, vol. 3, edited by CERES Science Team, pp. 135–176, 1995.

Minnis, P., J. K. Ayers, and S. P. Weaver, Surface-based observations of contrail occurrence frequency over the U.S., April 1993–April 1994, *NASA Ref. Publ. 1404*, 1997.

Minnis, P., D. F. Young, D. P. Garber, L. Nguyen, W. L. Smith, Jr., and R. Palikonda, Transformation of contrails into cirrus during SUCCESS, *Geophys. Res. Lett.*, *25*, 1157–1160, 1998a.

Minnis, P., D. P. Garber, D. F. Young, R. F. Arduini, and Y. Takano, Parameterizations of reflectance and effective emittance for satellite remote sensing of cloud properties, *J. Atmos. Sci.*, 3313–3339, 1998b.

Minnis, P., U. Schumann, D. R. Doelling, K. M. Gierens, and D. W. Fahey, Global distribution of contrail radiative forcing, *Geophys. Res. Lett.*, *26*, 1853–1856, 1999.

Nguyen, L., P. Minnis, J. K. Ayers, W. L. Smith Jr., and S. P. Ho, Intercalibration of geostationary and polar satellite data using AVHRR, VIRS, and ATSR-2 data, in *Proceedings of AMS 10th Conference on Atmospheric Radiation*, pp. 405–408, Am. Meteorol. Soc., Boston, Mass., 1999.

Payne, R. E., Albedo of the sea surface, *J. Atmos. Sci.*, *29*, 959–970, 1972.

Ponater, M., S. Brinkop, R. Sausen, and U. Schumann, Simulating the global atmospheric response to aircraft water vapour emissions and contrails: A first approach using a GCM, *Ann. de Geophys.*, *14*, 957–959, 1996.

Space Systems/Loral, *GOES I-M Databook, Revision 1, Ref. S-415-19*, Palo Alto, Calif., 1996.

Stuhlmann, R., P. Minnis, and G. L. Smith, Cloud bidirectional reflectance functions: A comparison of experimental and theoretical results, *Appl. Opt.*, *24*, 396–401, 1985.

Valero, F. P. J., P. Minnis, S. K. Pope, A. Bucholtz, B. C. Bush, D. R. Doelling, W. L. Smith Jr., and X. Dong, Absorption of solar radiation by the atmosphere as determined using satellite, aircraft, and surface data during the Atmospheric Radiation Measurement Enhanced Shortwave Experiment (ARESE), *J. Geophys. Res. 105*, 4743–4758, 2000.

D. P. Duda, Hampton University, NASA Langley Research Center, Mail Stop 420, 21 Langley Boulevard, Hampton, VA 23681-2199. (d.p.duda@larc.nasa.gov)

P. Minnis, Atmospheric Sciences, NASA Langley Research Center, Hampton, VA 23681.

L. Nguyen, Analytical Services and Materials, Inc., Hampton, VA 23666.